Chapter 2

Decomposing marine pressure data into a vector wavefield

Elastic modeling or migration of data recorded in a marine environment can be formulated as a coupled acoustic-elastic problem, with a common boundary condition at the sea floor. A simpler alternative is to solve only the elastic wave equation, with vanishing shear moduli within the water layer. To enable the application of this approach to real problems, it is necessary to transform the recorded scalar pressure wavefield into a vector particle-displacement field. In this chapter I derive a method to perform such vectorization of recorded marine data which is completely independent of the subsurface geology. Few assumptions are required for the theoretical justification of the method, the most important being that the depth of the cable is a smooth function of the receiver position. The wavefield vectorization is obtained through a simple, inexpensive, linear operation in the frequency-horizontal wavenumber domain. Except for attenuation of near-water-velocity dips good results were obtained when the method was applied to both synthetic and real data.

2.1 Introduction

Wave propagation in a marine environment can be separated into two parts: propagation through the water, for which the acoustic wave equation applies, and propagation in the subsurface strata, for which the elastic wave equation applies. While in liquids a scalar pressure wavefield is enough to properly describe the propagation of acoustic waves, in

solid layers a vector wavefield (particle displacement or particle velocity) is required to completely describe the motion of such waves. The coupling of the two wavefields can be achieved by the application of the continuity of the normal components of stress and displacement at the liquid-solid interface.

A different approach, on which the elastic modeling and migration method described in chapters 3 and 4 are based, is to solve only the elastic wave equation, distinguishing the solid and liquid regions only by their different elastic parameters. The application of the migration method is based on the assumption that the particle displacement vector field is known at the surface. However, a significant part of seismic reflection data collected nowadays comes from offshore surveys, where the seismic waves propagating in the water are recorded by pressure-sensitive phones arranged along a cable.

To apply the migration method to practical problems it is imperative that a vector displacement wavefield be obtained from the recorded pressure field. The next sections show that the conversion of the scalar recorded field into the elastic (vector) wavefield at the cable depth can be achieved by the application of a simple linear filter in the frequency-spatial wavenumber domain.

One of the critical points of the vectorization is the implicit separation of the downgoing and upcoming waves at the cable depth. In the most general case this separation cannot be done for standard marine data and the use of two cables at different depth has been advocated by several authors as a way to solve the separation problem (see e.g. Monk (1990) for a general discussion). I show that with the help of a few assumptions it is possible to solve the wavefield separation problem for standard marine surveys. Although the particular application described here (vectorization of the recorded field) does not seem to be critically sensitive to these assumptions, other applications such as deghosting may prove to be unfeasible under this separation scheme. The assumptions are that the water surface is nearly horizontal and that the cable depth is a smooth function of the receiver position. The cancellation of the total wavefield at some vertical wavenumbers introduces a set of singular strings in the vectorizer operator. However, it is possible to remove these singularities and to design a stable operator with a small loss of resolution in events with apparent velocities near the water velocity.

2.2 Theoretical background

2.2.1 Relating the pressure and displacement wavefields

The pressure wavefield $\phi(x,z,t)$ in a general heterogeneous, isotropic fluid medium, obeys the scalar wave equation

$$K(x,z)\,\nabla\cdot\,\{\frac{1}{\rho(x,z)}\nabla\phi(x,z,t)\}\;=\;\frac{\partial^2}{\partial t^2}\phi(x,z,t)$$

(Claerbout, 1985), which in the frequency domain is represented by

$$K(x,z)\,\nabla\cdot\,\{\frac{1}{\rho(x,z)}\nabla\phi(x,z,\omega)\}\;=\;-\omega^2\phi(x,z,\omega). \tag{2.1}$$

In the equations above, K and ρ represent the bulk modulus and the density of the media, respectively.

The P wave particle-displacement vector field $\mathbf{u}$ is related to the pressure by the following expression:

$$\phi(x,z,\omega)\;=\;-K(x,z)\,\nabla\cdot\mathbf{u}(x,z,\omega). \tag{2.2}$$

Substituting equation (2.2) into equation (2.1) leads to

$$\nabla\cdot\mathbf{u}(x,z,\omega)\;=\;\nabla\cdot\,\{\frac{1}{\omega^2\rho(x,z)}\,\nabla\phi(x,z,\omega)\}. \tag{2.3}$$

Recalling that, in general, the vector field $\mathbf{u}$ can be represented by the sum of a gradient potential with a rotational potential, and that in the recording medium (water) the displacement field must be irrotational, equation (2.3) can be simplified to

$$\mathbf{u}(x,z,\omega)\;=\;\frac{1}{\omega^2\rho(x,z)}\,\nabla\phi(x,z,\omega). \tag{2.4}$$

This equation relates the displacement vector field to the scalar pressure field for general liquid media.

Difficulties arise in the computation of the pressure gradient when equation (2.4) is to be applied to standard offshore data. Because conventional marine datasets are collected with a single cable, positioned nearly parallel to the water surface, the horizontal derivative of the pressure field can be easily evaluated, while the absence of vertical sampling hinders the direct evaluation of the vertical derivative. In the next sections I derive a method for evaluation of the pressure gradient from data acquired with a standard geometry.

2.2.2 Decomposing the recorded pressure field into the downgoing and upcoming wavefields

Most of the treatment that follows is carried out either in the τ-p or in the ω-κ_x domain. To simplify the analysis, avoiding the unnecessary intrusion of convolutions along the κ_x axis, the discussion focuses on the points in space where the wavefield is measured, that is, at the points $(x, z = z_0)$ where z_0 is the cable depth. At these points the bulk moduli and density are constant and known: $K(x, z_0) = K$, and $\rho(x, z_0) = \rho$.

The pressure field ϕ at any position of the space can be represented as the superposition of an upward propagating wavefield ϕ_u with a downward propagating wavefield ϕ_d:

$$\phi(x, z_0, \omega) \;=\; \phi_u(x, z_0, \omega) \;+\; \phi_d(x, z_0, \omega). \tag{2.5}$$

Continuation of these wavefields in the frequency-horizontal wavenumber domain (ω-κ_x) is controlled by the following equations:

$$\frac{\partial}{\partial z}\phi_u(\kappa_x, z_0, \omega) \;=\; -i\,\kappa_z\,\phi_u(\kappa_x, z_0, \omega) \tag{2.6}$$

$$\frac{\partial}{\partial z}\phi_d(\kappa_x, z_0, \omega) \;=\; i\,\kappa_z\,\phi_d(\kappa_x, z_0, \omega), \tag{2.7}$$

where κ_z is the vertical wavenumber, which relates to the horizontal slowness p through the dispersion relation

$$\kappa_z \;=\; \omega\sqrt{\frac{\rho}{K} - p^2} \;=\; \omega\sqrt{\frac{\rho}{K} - \left(\frac{\kappa_x}{\omega}\right)^2}. \tag{2.8}$$

To separate these two wavefields, we must make the following assumptions:

- The water-air reflection coefficient[1] is -1.

- The water surface is nearly horizontal.

- The cable depth is a smooth function of the receiver position.

[1]This is not actually a requirement but a reasonable practical choice that considerably simplifies the mathematical treatment.

Under these assumptions, the upcoming and downgoing fields can be related by a simple time shift equation in the τ-p domain:

$$\phi_d(p, z_0, \tau) \;=\; -\,\phi_u(p, z_0, \tau - 2z_0 q(p)), \tag{2.9}$$

where q is the vertical slowness. When the source is located below the cable equation (2.9) can be applied without restrictions, and the only event for which it doesn't hold perfectly true, for cases in which the source is above the cable, is the direct wave.

Substituting equation (2.9) into equation (2.5), both in the ω-p domain, we obtain

$$\phi(p, z_0, \omega) \;=\; \phi_u(p, z_0, \omega)\,[1 - \exp\,(i2z_0\omega\sqrt{\rho/K - p^2})]; \tag{2.10}$$

which results in the following equations for separation of the two wavefields:

$$\phi_u(p, z_0, \omega) \;=\; \frac{\phi(p, z_0, \omega)}{1 - \exp(i2z_0\omega\sqrt{\rho/K - p^2})}, \tag{2.11}$$

$$\phi_d(p, z_0, \omega) \;=\; \frac{\phi(p, z_0, \omega)}{1 - \exp(-i2z_0\omega\sqrt{\rho/K - p^2})}. \tag{2.12}$$

2.2.3 Calculating the pressure gradient in the ω-κ_x domain

It is easy to obtain the horizontal component of the gradient in the ω-κ_x domain

$$\frac{\partial}{\partial x}\phi(x, z_0, \omega) \;\overset{x \rightarrow \kappa_x}{\Longrightarrow}\; i\,\kappa_x\,\phi(\kappa_x, z_0, \omega). \tag{2.13}$$

To obtain the vertical component however, it is necessary to uncouple the downgoing and upcoming components. Taking the vertical derivative of equation (2.5), moving to the ω-κ_x domain, and using the relations in (2.7), we get

$$\frac{\partial}{\partial z}\phi(\kappa_x, z_0, \omega) \;=\; -i\,\kappa_z\,\phi_u(\kappa_x, z_0, \omega) \;+\; i\,\kappa_z\,\phi_d(\kappa_x, z_0, \omega). \tag{2.14}$$

Finally, equations (2.11) and (2.12) can be substituted into equation (2.14) to give

$$\frac{\partial}{\partial z}\phi(\kappa_x, z_0, \omega) \;=\; \kappa_z\,\cot(z_0\kappa_z)\,\phi(\kappa_x, z_0, \omega). \tag{2.15}$$

A first glance at equation (2.15) shows that it has a set of singular hyperbolic strings in the ω-κ_x plane, which are defined by

$$\omega_n(\kappa_x) = \pm\sqrt{\left(\frac{K}{\rho}\right)\left[\left(\frac{n\pi}{z_0}\right)^2 + \kappa_x^2\right]}, \tag{2.16}$$

and which correspond to vertical wavelengths of $\frac{2\,z_0}{n}$. For waves with these wavelengths, the downgoing and upcoming fields cancel each other at the cable depth (assuming perfect reflection at the water's surface), and the result is a zero in the recorded wavefield. Nevertheless, neither the cancellation of the wavefield, nor the singularities in the operator restrict the complete recovery of the displacement field because, fortunately the product of the singular operator by the null wavefield has a definite limit that can be found using L'Hospital's rule.

In the neighborhood of these strings, the vertical component of the pressure gradient is given by

$$\lim_{\omega \to \omega_n(\kappa_x)} \frac{\partial}{\partial z}\, \phi(\kappa_x, z_0, \omega) \;=\; \frac{\omega}{z_0} \frac{\partial}{\partial \omega}\, \phi(\kappa_x, z_0, \omega). \tag{2.17}$$

2.2.4 The vectorizer operator

Using the partial derivatives defined by equations (2.15), (2.17), and (2.13), we can express equation (2.4) as a simple linear operation in the ω-κ_x domain:

$$\mathbf{u}(\kappa_x, z_0, \omega) \;=\; \tilde{\boldsymbol{\kappa}}(\kappa_x, z_0, \omega)\; \phi(\kappa_x, z_0, \omega), \tag{2.18}$$

where $\tilde{\boldsymbol{\kappa}}$ is the vectorizer operator, whose components are

$$\tilde{\kappa_x} \;=\; \frac{i}{\rho \omega^2}\; \kappa_x, \tag{2.19}$$

(2.20)

$$\tilde{\kappa_z} \;=\; \begin{cases} \dfrac{1}{\rho\omega^2}\; \cot(z_0 \kappa_z)\; \kappa_z & \text{for} \quad \omega \neq \omega_n(\kappa_x) \\[2ex] \dfrac{\pi^2 K}{z_0^3 \rho^2}\; \dfrac{n^2}{\omega_n^3}\; \dfrac{\partial}{\partial \omega} & \text{for} \quad \omega = \omega_n(\kappa_x). \end{cases} \tag{2.21}$$

The horizontal and vertical components of the operator represented in equations (2.19) and (2.21), are illustrated in Figure 2.1 in both the frequency-wavenumber and the space-time domains. It is important to realize that while Figures 2.1a and 2.1c multiply the Fourier-transformed pressure field, 2.1e multiplies the frequency-derivative of the same transformed field. Therefore, while 2.1b and 2.1d should be convolved with the pressure field, 2.1f should be convolved with the time-scaled pressure field (which is, in practice, equivalent to convolving it with the wavefield corrected for 2-D divergence). Only the non-zero parts of the operator are represented in the figure, that is, the imaginary parts in 2.1a and 2.1f and the real parts in the other four images.

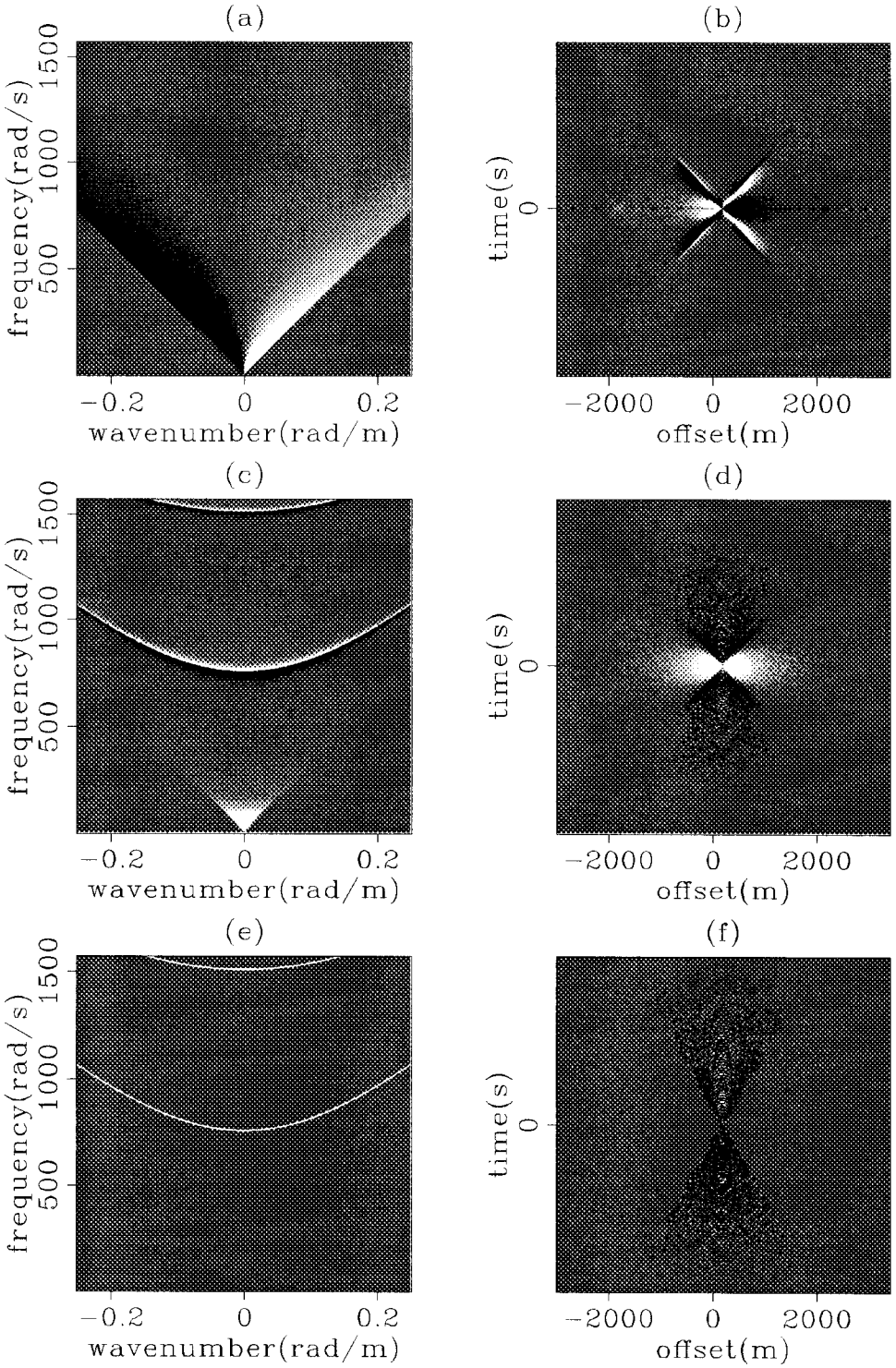

FIG. 2.1. Wavefield vectorizer operator. (a) $\tilde{\kappa_x}$ in ω-κ_x domain. (b) $\tilde{\kappa_x}$ in x-t domain. (c) $\tilde{\kappa_z}$ in ω-κ_x domain (for $\omega \neq \omega_n(\kappa_x)$). (d) $\tilde{\kappa_z}$ in x-t domain (for $\omega \neq \omega_n(\kappa_x)$). (e) $\tilde{\kappa_z}$ in ω-κ_x domain (for $\omega = \omega_n(\kappa_x)$). (f) $\tilde{\kappa_z}$ in x-t domain (for $\omega \neq \omega_n(\kappa_x)$).

It is interesting to observe that the impulse response of $\tilde{\kappa_x}$ in the space-time domain clearly resembles the convolution of a second derivative in time (with reversed sign) with a first derivative in space. Inverse theory tell us that the first approximation to the inverse is the conjugate operator, and in this case we find that the double time integration coming from the $1/\omega^2$ term resembles the negative second time derivative in the time domain.

2.3 Application of the method to synthetic and real data

To test the resolution of the method I generated a synthetic dataset using the elastic finite differences algorithm described in chapter 3. The pressure wavefield is obtained at each time step from the displacement field by taking the divergence of the displacement field and multiplying by the bulk modulus (Equation (2.2)). Both the displacement and pressure wavefields were "recorded" at the gridpoints associated with the recording cable. Figure 2.2a shows the structurally complex model used to generate the data and Figure 2.2b shows the recorded pressure field corresponding to a shot gather which has a diversity of events which include non-hyperbolic reflections, diffractions, and converted modes.

Figure 2.3 compares the *true* (computed by the modeling algorithm) horizontal component of the displacement field with the horizontal component *retrieved* from the pressure field using the vectorizer operator. The same comparison for the vertical component is shown in Figure 2.4. The result from subtracting the true from the retrieved fields is shown in Figure 2.5. The differences are larger at the near and far offsets because of the missing information associated with the finite aperture of the data. The direct wave, as well as other events with similar stepout, are also not correctly retrieved because of the taper that needs to be applied near the boundary with the evanescent region ($\kappa_x = \omega/v$). This taper is important not only because of the evanescent region but also because the direct wave is not correctly handled by Equation (2.18) since the source in this synthetic case (and also in the field data example) is located above the cable. As one would expect, the fit between the true and retrieved wavefields is better for the horizontal component because it is much easier to compute the spatial derivative along the direction in which the data is collected than orthogonally to that direction.

Figure 2.6 shows the time-spectra of a near and far offset of the retrieved and true

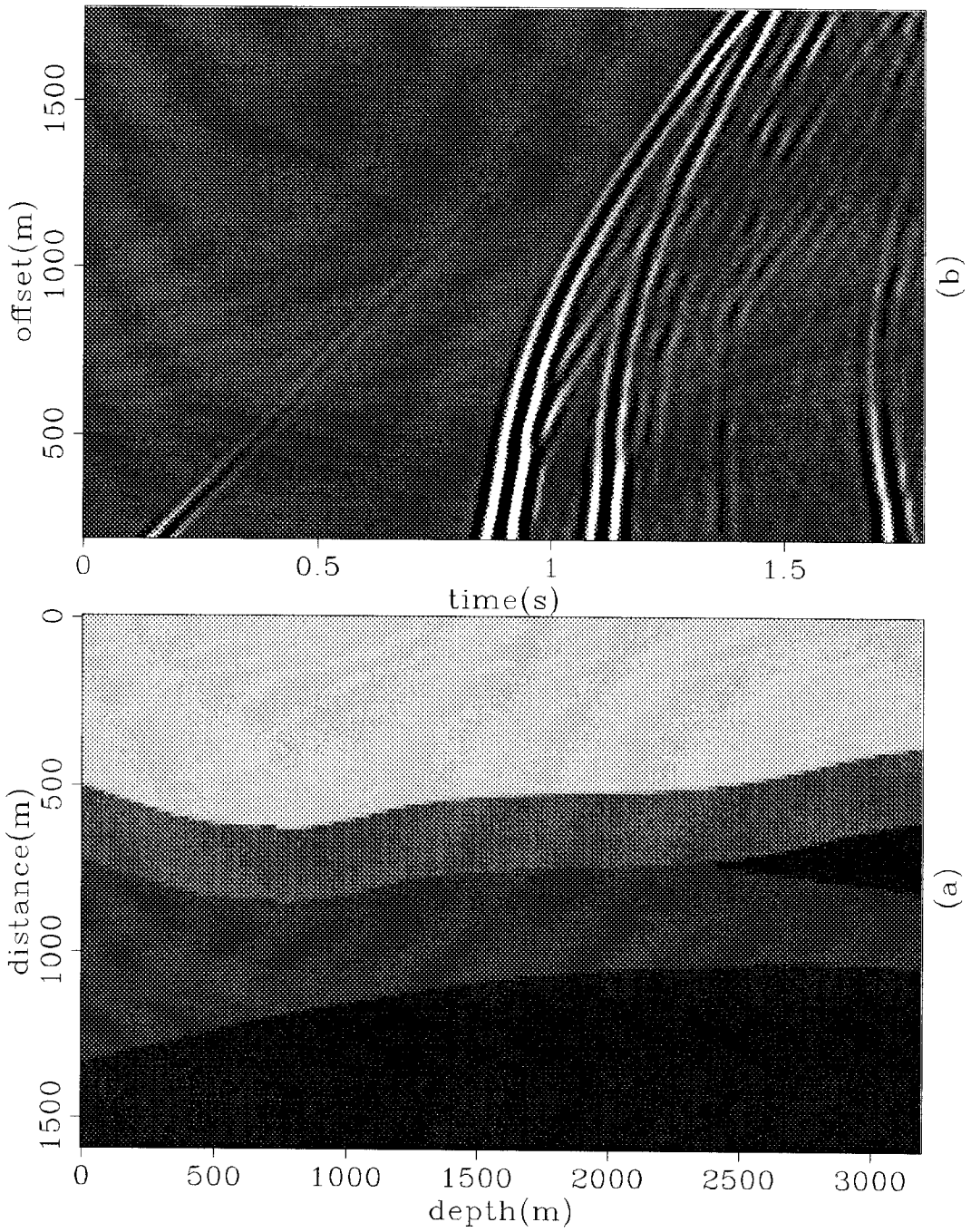

FIG. 2.2. (a) P-wave velocity component of the elastic model used to generate the synthetic data. (b) Pressure field at depth 12.5 meters, corresponding to a common shot gather generated by an elastic modeling algorithm using the model shown in (a).

vertical components. This figure shows that the frequencies where the zeros of the spectrum are located were correctly estimated, but their amplitudes (i.e., how far they are from the unit circle) are slightly different from the correct ones. Also visible is the fact that the spectrum of the estimated component is slightly more red (more low frequency content) than the spectrum of the true component. This is not surprising since the vertical component of the vectorizer operator clearly favors the low-frequency part of the spectrum.

The method was also tested on an offshore dataset from Brazil, which was recorded in an area with an irregular ocean floor, and with slightly structured subsurface geology. According to the observer's report, the cable depth ranged from 8 to 12 meters, with an average of 10 meters. Moderately strong winds were also reported resulting in a non-stationary level of the sea surface. Figure 2.7a shows the common shot gather used in the tests and Figure 2.7b shows low frequency version of the same gather.

Figure 2.8 shows the resulting displacement vector field obtained with the method described in this chapter. A first glance at this figure reveals a striking similarity between the the horizontal component and the unfiltered pressure field in Figure 2.7a and between the vertical component and the filtered pressure field in 2.7b. There are however important differences in the amplitude and phase of these "similar" wavefields. Low dip events which are visible in the unfiltered pressure field are absent or largely attenuated in the horizontal component. Most of the energy in the horizontal component is concentrated at the far offsets. The first sea floor multiple is more continuous (at the far offsets) and has a different phase in the horizontal component than in the pressure field. Most events have better lateral continuity in the vertical component than in the filtered pressure field. The strong reflection that lies just below the sea floor reflection at the longest offset of the filtered pressure field has the same phase as the horizontal component at the far offsets and the same phase as the vertical component at intermediate and near offsets. Finally, we notice that as a side-effect, the gap of two traces in the original pressure field has been filled in the components of the displacement field.

To understand why the dominant frequency is lower in the vertical component than in the horizontal component it is important first to make a distinction between the zeroes in the spectrum of the pressure field and the zeroes in the spectrum of the horizontal and vertical components of the displacement field. The zeroes in the spectrum of the pressure field coincide with the zeroes in the spectrum of the horizontal component and correspond

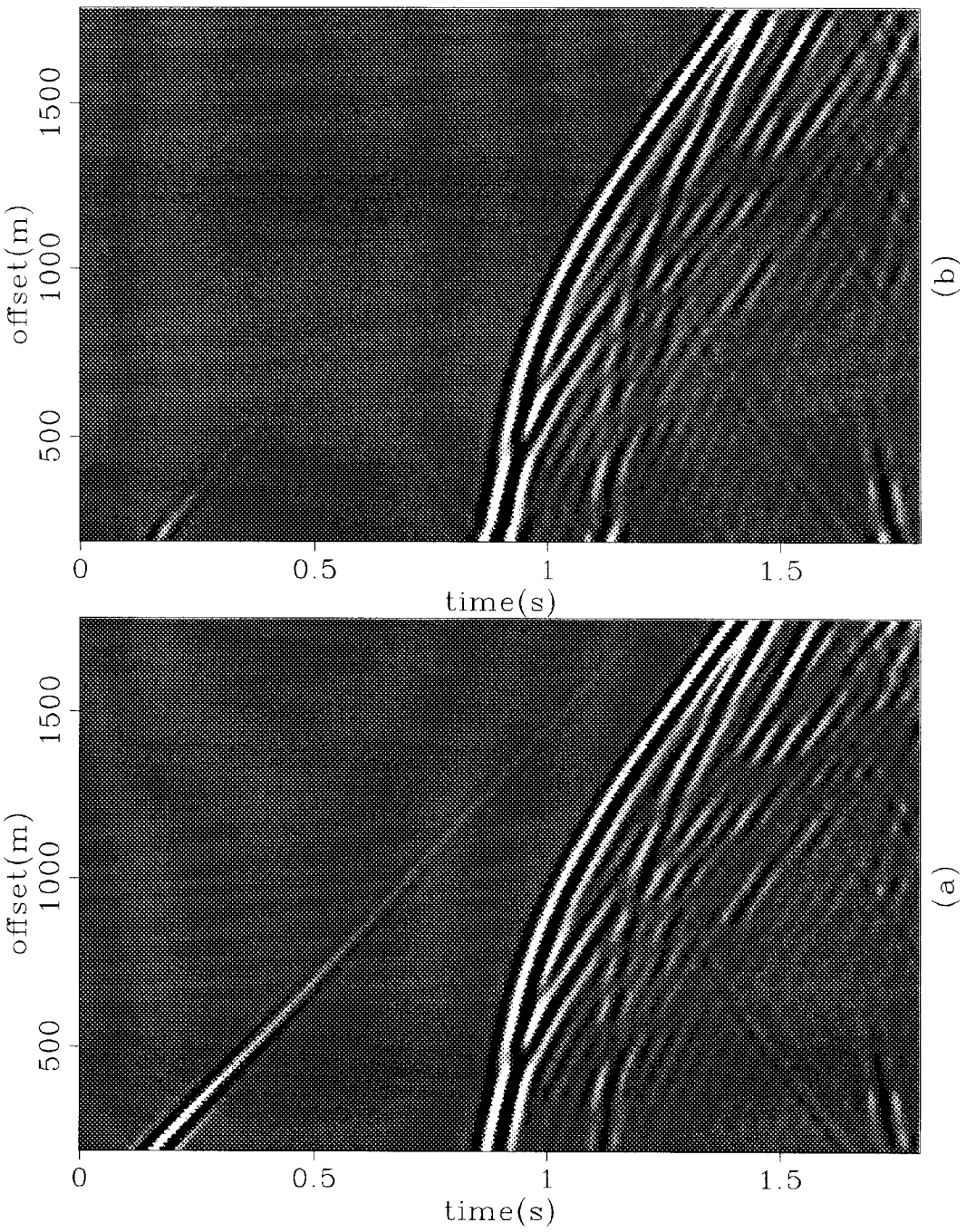

FIG. 2.3. (a) Horizontal component of the displacement field generated by an elastic modeling algorithm. The pressure field in Figure 2.2 was obtained from this component and the vertical component shown in Figure 2.4a by a divergence operation. (b) Horizontal component retrieved from the pressure field using the vectorizer operator.

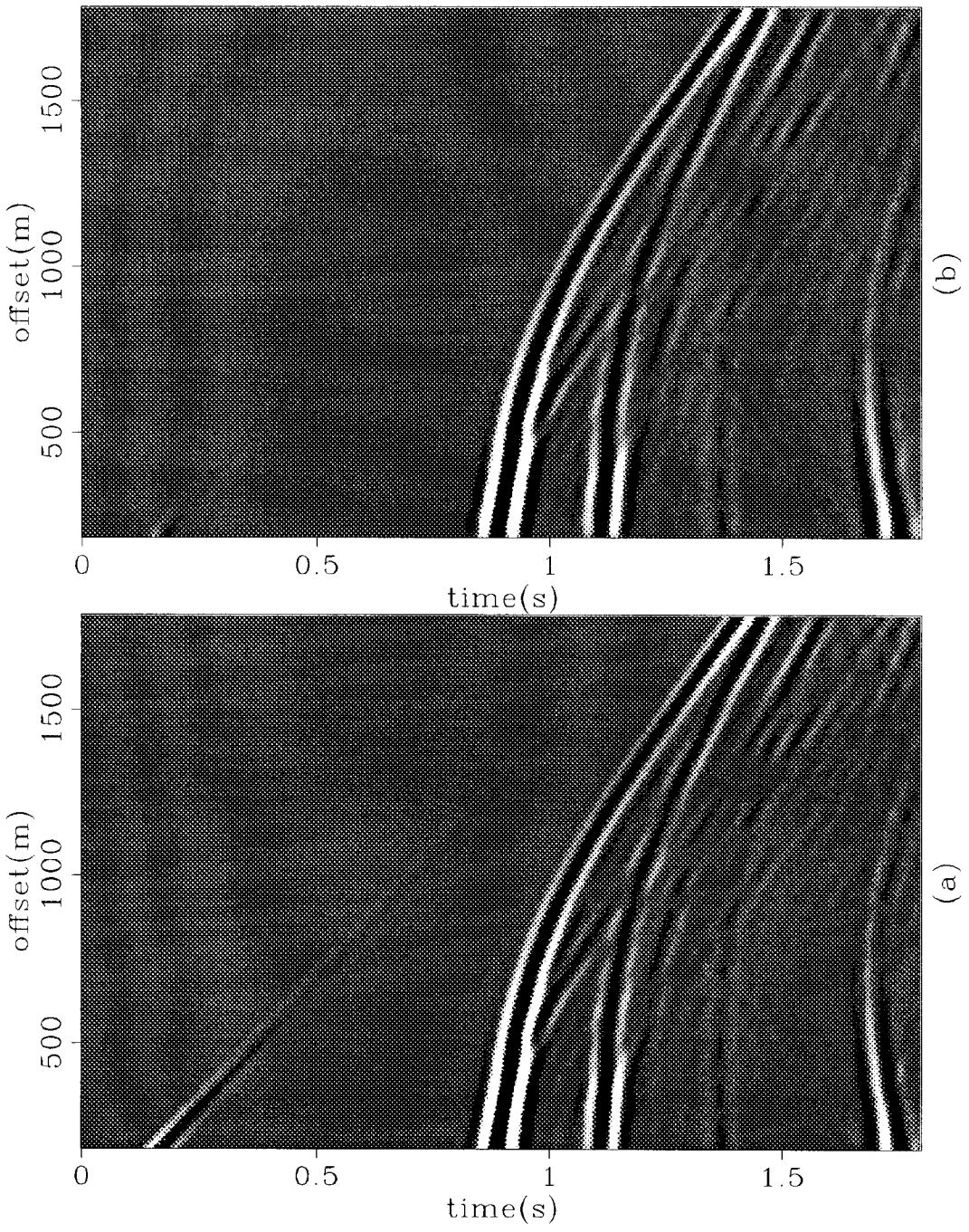

FIG. 2.4. (a) Vertical component of the displacement field generated by an elastic modeling algorithm. (b) Vertical component retrieved from the pressure field using the vectorizer operator.

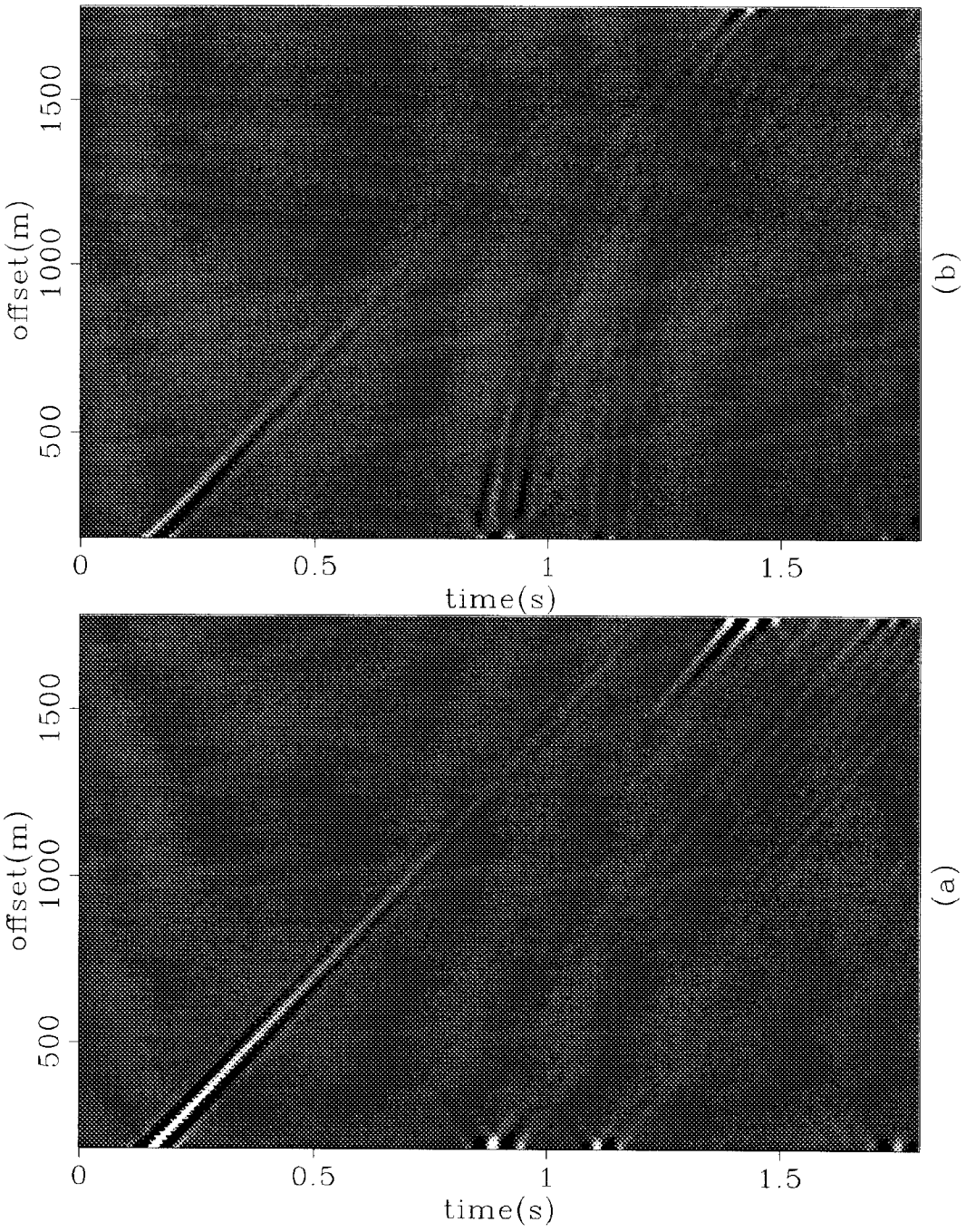

FIG. 2.5. (a) Difference between the true and retrieved horizontal components shown in Figure 2.3. (b) Difference between the true and retrieved vertical components shown in Figure 2.4.

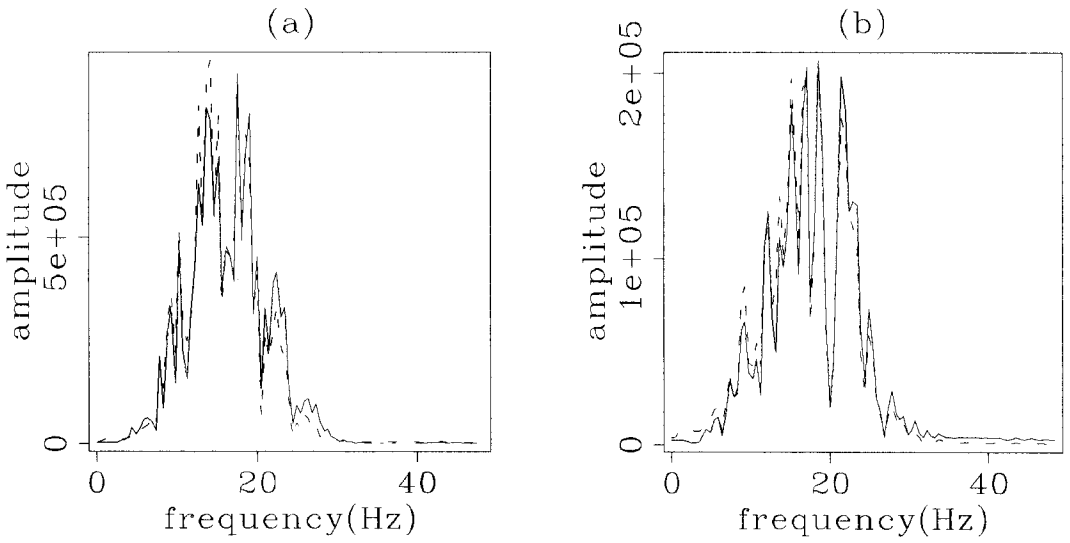

FIG. 2.6. Comparison between the time-spectra of the true and retrieved vertical components shown in Figure 2.4 for (a) the fifth offset and (b) the 80th offset.

to wavelengths which are submultiples of twice the cable depth (i.e. $n\lambda = 2z_0$). On the other hand, the zeroes of the vertical component are associated with vertical wavelengths that obey the equation $(n + 1/2)\lambda = 2z_0$. For these particular field data ($z_0 = 10$ meters, $v = 1500$ m/s), and for *vertical incidence*, the first zero of the vertical component is located at $f = v/(4z_0) = 37.5$ Hz, while the first zero of the horizontal component and of the pressure field (after the zero frequency) is located at $f = 75$ Hz. For non-vertical incidence, these notch frequencies increase with the secant of the incidence angle. Figure 2.9 shows the smoothed spectra of the pressure field and the two components of the displacement field for a near-offset trace and a far-offset trace. Because of the zero at 37.5 Hz the vertical component has a lower bandwidth and a lower fundamental frequency than the horizontal component and the pressure data. A comparison between the near and far traces shows that the colors of the three wavefields become more similar as the propagation angle increases. As expected the vertical component has a pole at 75 Hz, where the horizontal component vanishes. This high-frequency part of the spectrum was filtered out of the field data examples for several reasons: some high-dip events become spatially aliased at these frequencies; the signal-to-noise ratio is lower in this part of the spectrum; and keeping this isolated pick in the spectrum introduces a monochromatic pattern in the data.

Although a direct comparison with the true vector field is not possible in this field data

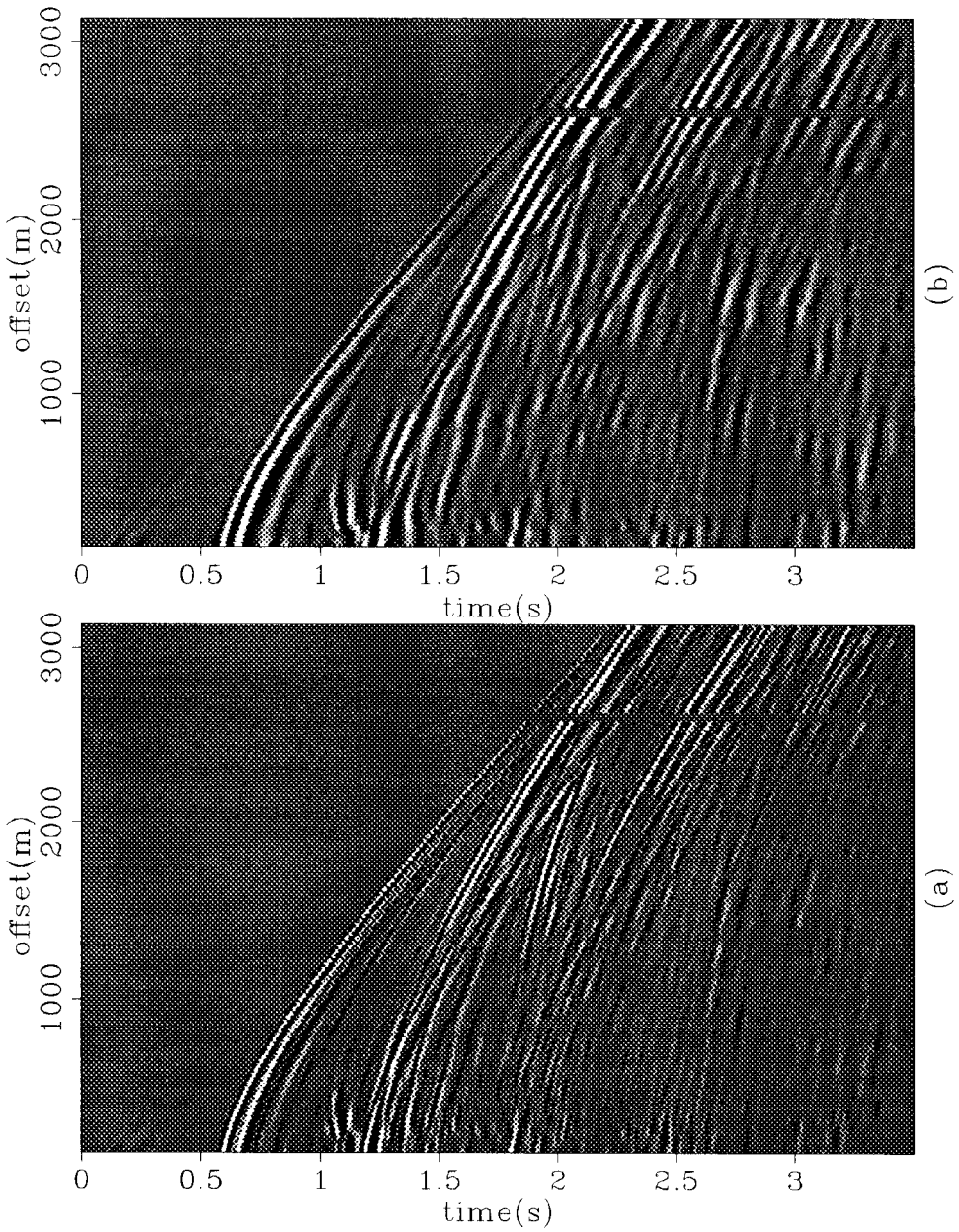

FIG. 2.7. (a) Common shot point gather from Brazil. The average depth of the cable is 10 meters. (b) The same gather shown in (a) after the application of a high-cut filter.

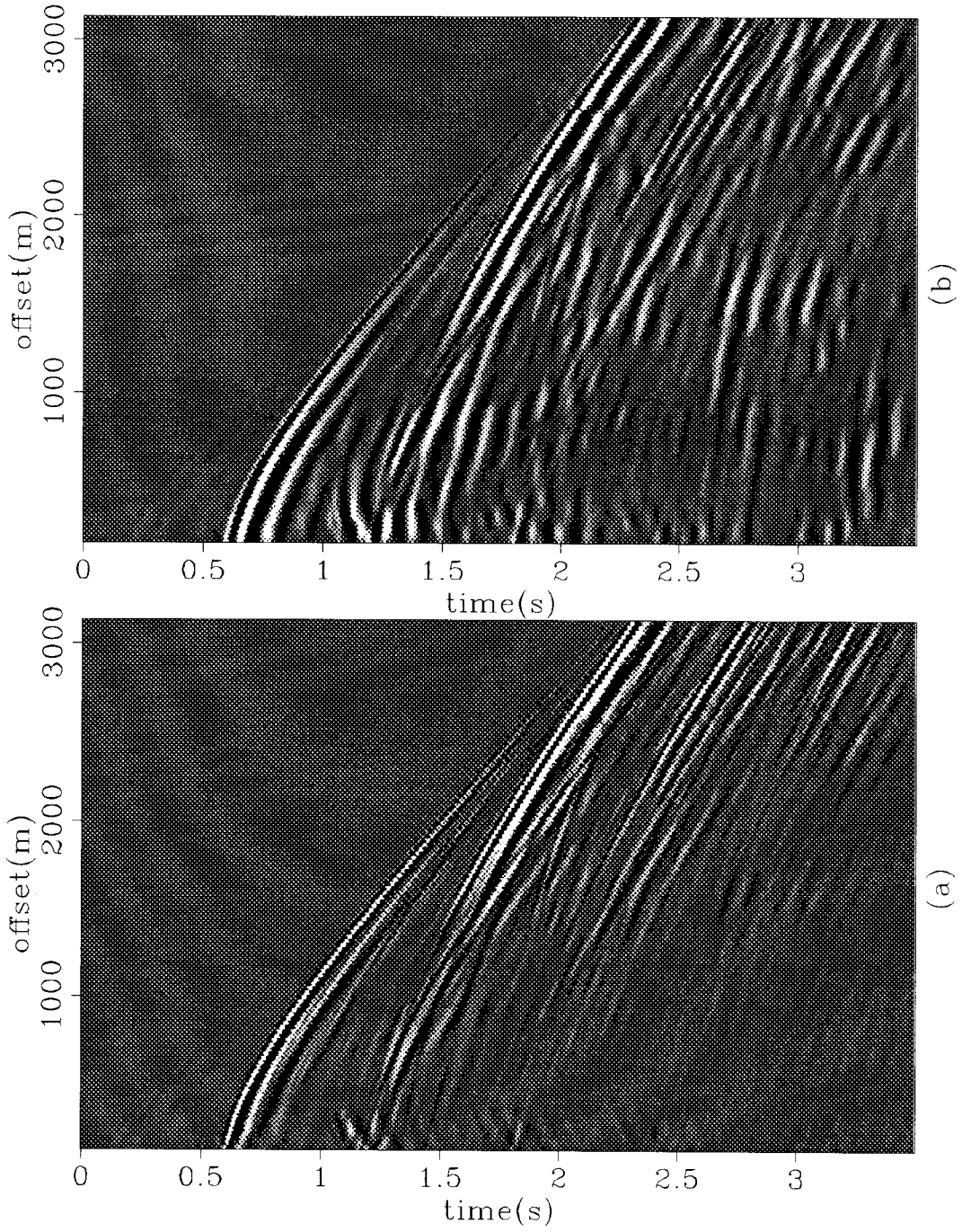

FIG. 2.8. (a) Horizontal and (b) vertical components of the displacement field retrieved from the pressure field shown in Figure 2.7.

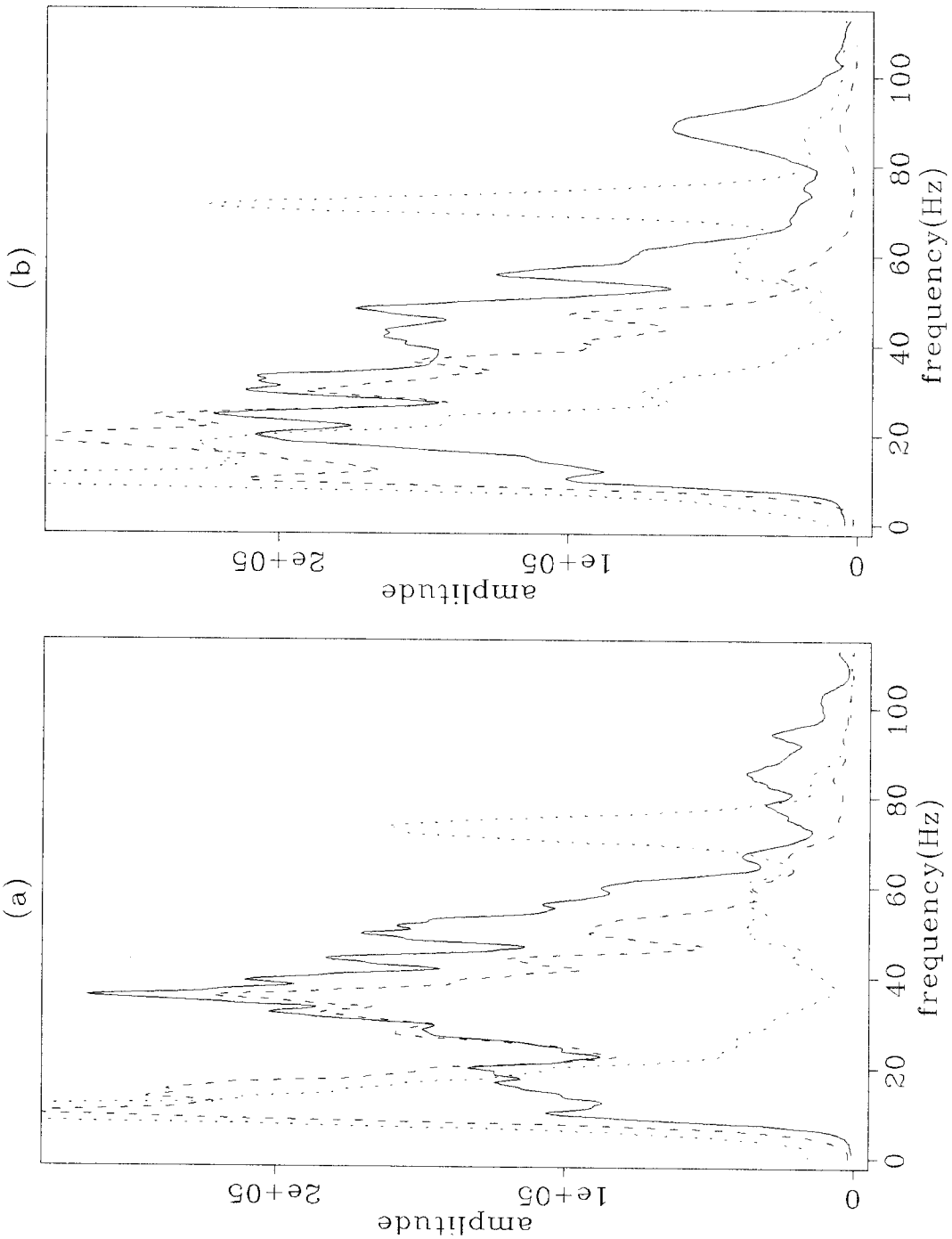

FIG. 2.9. Smoothed spectra of the pressure field (**continuous** line) , the horizontal component (**dashed** line) and the vertical component (**dotted line**) for (a) a near offset trace and (b) a far offset trace.

example, there are some tests that can show at least the self-consistency of the results. One test involves the sensitivity of the method to errors in the correct depth of the cable.

In the space-time domain each point of the cable will "see" at the same time an upcoming wavefield arriving at an angle θ_{up} and a downgoing wavefield arriving at an angle θ_{down}. If the subsurface has some degree of lateral smoothing, then $\theta_{up} \approx -\theta_{down}$ and the amplitude of the downgoing wave will be a delayed version of the amplitude of the incident wave with reversed polarity. The resulting superposition will have an apparent arrival angle (as measured by the displacement field direction) that covers the full range from $-\theta$ to θ. In addition the total wavefield will have maximum amplitude at the apparent angle $\theta = 0$.

Figure 2.10 shows the absolute apparent angle panels generated from the elastic wavefields estimated from the data in Figure 2.7 using six different values of cable depth. The first two panels are predominantly dark with a few white sparks, which indicates very small apparent angles, that is, almost vertical arrivals. The last panel starts to became dark again and lose lateral coherence, which indicates random apparent angles. The three panels corresponding to cable depths of 10, 14, and 18 meters give the more coherent images, which is consistent with the values reported in the field observer's log (14 ± 2).

2.4 Summary

To allow the implementation of the elastic reverse-time migration algorithm for marine datasets it is necessary to convert the recorded pressure field into a vector displacement field. Although the two wavefields are related by a very simple equation (the displacement field is proportional to the gradient of the pressure field), it is not possible in practice to directly apply this equation to most real cases. The reason for this practical difficulty is that vertical component of the gradient cannot be directly computed in the space domain because the typical marine geometry comprises a single horizontal line of receivers. However, with very few assumptions it is possible to separate the upcoming and downgoing components of the wavefield and obtain an operator in the frequency-horizontal wavenumber domain that can effectively compute the pressure gradient. Results with synthetic and real data demonstrate the applicability of the method.

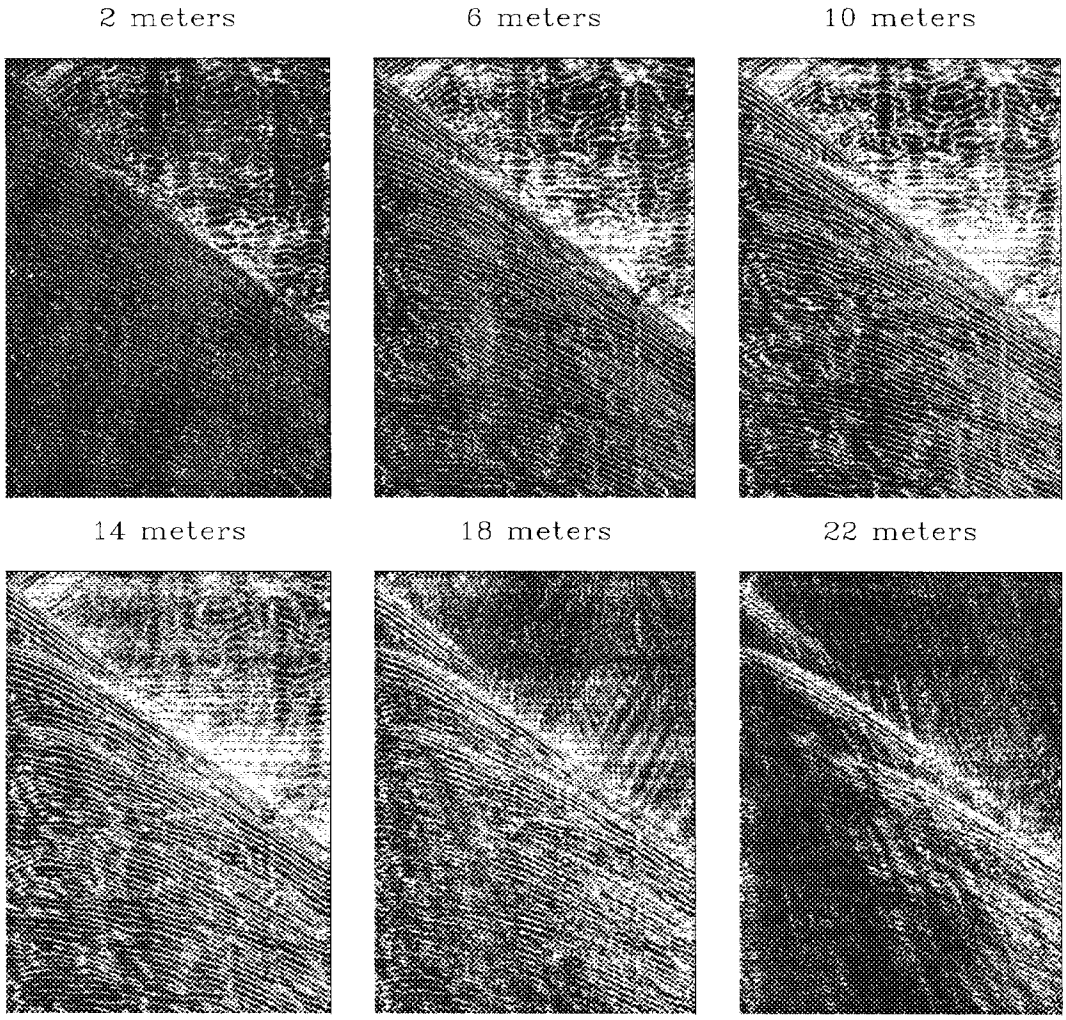

FIG. 2.10. Apparent-angle coherence analysis of the data shown in Figure 2.7. Each panel corresponds to an arriving angle panel for the elastic wavefield obtained with different values of cable depth.